

## Holographic optical coherence imaging of tumor spheroids

P. Yu<sup>a)</sup> and M. Mustata

*Department of Physics, Purdue University, 1396 Physics Building, West Lafayette, Indiana 47907-1396*

J. J. Turek

*Department of Basic Medical Sciences, School of Veterinary Medicine, Purdue University, West Lafayette, Indiana 47907-1246*

P. M. W. French

*Department of Physics, Imperial College of Science, Technology and Medicine, London, SW7 2BZ United Kingdom*

M. R. Melloch

*School of Electrical and Computer Engineering, Purdue University, West Lafayette, Indiana 47907-2035*

D. D. Nolte

*Department of Physics, Purdue University, 1396 Physics Building, West Lafayette, Indiana 47907-1396*

(Received 10 February 2003; accepted 13 May 2003)

We present depth-resolved coherence-domain images of living tissue using a dynamic holographic semiconductor film. An AlGaAs photorefractive quantum-well device is used in an adaptive interferometer that records coherent backscattered (image-bearing) light from inside rat osteogenic sarcoma tumor spheroids up to 1 mm in diameter *in vitro*. The data consist of sequential holographic image frames at successive depths through the tumor represented as a visual video “fly-through.” The images from the tumor spheroids reveal heterogeneous structures presumably caused by necrosis and microcalcifications characteristic of human tumors in their early avascular growth. © 2003 American Institute of Physics. [DOI: 10.1063/1.1594830]

The search for clinical situations where optical (nonionizing) imaging can replace x-ray imaging without sacrificing diagnostic information has been significantly aided by the fact that light in the near infrared is not strongly absorbed as it propagates through most biological tissue, even though it is significantly scattered.<sup>1</sup> This ability of light to penetrate tissue is the basis of coherence-domain imaging.<sup>2–4</sup> Optical coherence tomography (OCT)<sup>5</sup> uses interferometric scanning to record laser ranging for a point-by-point lateral scan, demodulating the coherent contributions of the interferogram, and providing a depth scan at each surface point from which volumetric reconstructions are computed.

In this letter, we use photorefractive quantum wells (PRQW) to holographically demodulate the coherent signal and acquire full-frame images from an adjustable depth (set by the reference delay). The key element in the interferometer is the dynamic holographic film<sup>6</sup> that acts as a coherence filter passing full-frame coherent image-bearing light to a camera, while rejecting scattered background.<sup>7–10</sup> Because of its use as a simple filter in the optical imaging path, it provides *en face* images without computed reconstructions. It is depth-gated, making it possible to fly through scattering tissue as a succession of optical sections. Here we demonstrate *in vitro* fly-throughs of living tissue: rat osteogenic sarcoma tumor spheroids.

The optical coherence imaging (OCI) system is composed of a low-coherence source (a mode-locked 120 fs pulse duration 100 MHz repetition rate Ti:sapphire laser) and an imaging Mach–Zehnder interferometer. A PRQW device

performs as the adaptive beam combiner of the interferometer,<sup>6</sup> and a charge coupled device (CCD) camera records holographic coherence images [shown schematically in Fig. 1(a)]. The active area in the quantum-well device consists of 100 layers of 70 Å GaAs and 50 Å AlGaAs multiple quantum wells. After proton implantation, the devices become photorefractive through the Franz–Keldysh electro-optic effect of the quantum-confined excitons. Details of the fabrication and electro-optic properties of PRQW devices are found in Ref. 11. The center wavelength of the laser was tuned to 840 nm with a bandwidth of 12 nm, which covers the excitonic spectral bandwidth of the quantum well. A dc electric field of 10 kV/cm applied in the plane of the device allows so-called transverse-field operation of the PRQW device. The hologram refresh rate is on the order of 100 kHz, making the interferometer insensitive to mechanical motion.<sup>12</sup>

A degenerate four-wave mixing arrangement was used to acquire fly-through images, as shown in Fig. 1(b). Two beams, one from the sample and the other a reference, cross at an angle of 2.3° illuminating an area 1 by 3 mm<sup>2</sup> and generating a spatial carrier interference pattern with a fringe spacing of 20 μm on the PRQW. The transverse resolution of the system was 20 μm, measured using holograms of a USAF test chart, and the depth resolution was 35 μm measured by placing a mirror at the sample position. The total intensity at the PRQW was 6 mW/cm<sup>2</sup> with a reference and signal intensity ratio of 6. The hologram was read out by the reference pulse. A square aperture placed after the PRQW was used to block the zero-order and transmit the first-order diffracted signal from the reference beam onto the CCD

<sup>a)</sup>Electronic mail: pingyu@physics.purdue.edu

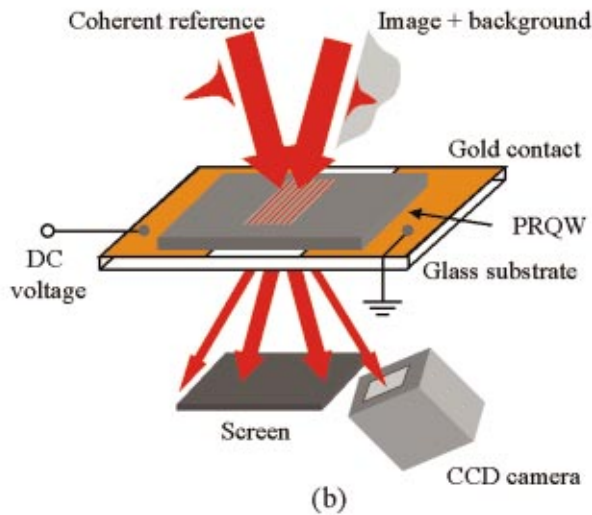
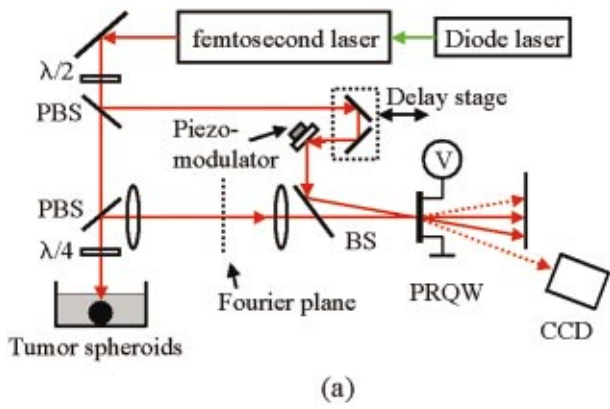


FIG. 1. (Color) (a) Optical coherence imaging experimental arrangement. PBS: polarization beam splitter. BS: 50% beam splitter. (b) Schematic of the PRQW in degenerate four-wave mixing.

camera. With this configuration, the system is background-free because the multiply scattered light from the tissue appears mainly in the zero order, which is blocked. We used a vibrating mirror controlled by a piezomodulator in the reference beam to time-average interpixel laser speckle. The mirror vibrated at 1 kHz and produced lateral speckle movement of about  $20 \mu\text{m}$ . Because the photorefractive quantum well has a fast response time (typically 100 kHz, depending on the total intensity on the device), the moving fringes caused

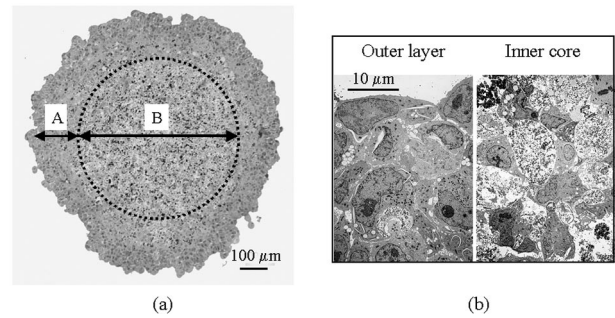


FIG. 2. (a)  $1\text{-}\mu\text{m}$ -thick section of a tumor spheroid with an outer shell of viable cells and an inner core of apoptotic cells and necrosis. (b) Transmission electron micrograph of outer living spheroid shell and inner core with areas of necrosis and mineralization.

by the vibrating mirror are quasistatic, and the four-wave mixing efficiency is not affected by the moving fringes. But the low-frequency mirror motion time averages the interpixel speckle on the CCD camera over the 500 ms acquisition time of a frame.

The tumor spheroids used in these experiments consisted of rat osteogenic sarcoma UMR-106 cells. The cells were cultured in nontissue-culture plastic dishes that cause the tumor cells to form small spheroids in 7–10 days, which were then transferred to a rotating bioreactor where they were maintained in suspension. The spheroids were grown up to 1 mm in diameter, thus large enough to simulate the thickness of different mammalian tissue (skin epidermis is  $70\text{--}120 \mu\text{m}$  in thickness over most of the human body).

As tumor spheroids are cultured, they undergo cell apoptosis/necrosis in their center in a manner similar to naturally occurring nodular tumors. In addition, if certain tumor cell lines are used, the spheroids develop microcalcifications that are similar to those that occur in human intraductal carcinomas of the breast.<sup>13–15</sup> These features can be seen in conventional thin sections of tumor spheroids, where the tumor spheroids were chemically crosslinked and embedded in epoxy resin. Using conventional microscopy, serial sections of  $1 \mu\text{m}$  thickness were stained with toluidine blue and digital images were acquired. The optical micrograph of a  $1 \mu\text{m}$  section of a tumor spheroid in Fig. 2(a) shows an outer shell of viable cells and an inner core of apoptotic cells and necrosis. Many cells can be recognized as connected structures

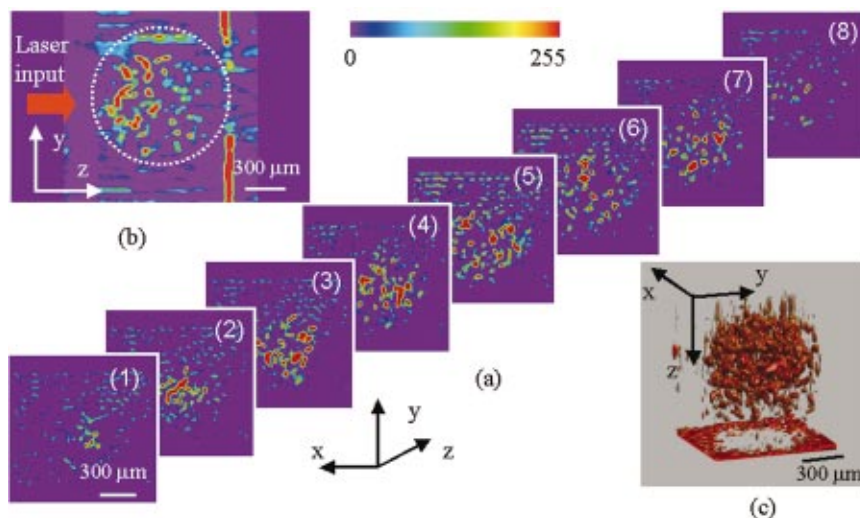


FIG. 3. (Color) (a) Holograms from different depths of the tumor spheroid. (b) Cross section in the  $y\text{-}z$  plane. (c) 3D view reconstructed from optical coherence imaging. The  $z$  axis represents depth. The  $x\text{-}y$  plane is the holographic image plane of OCI.

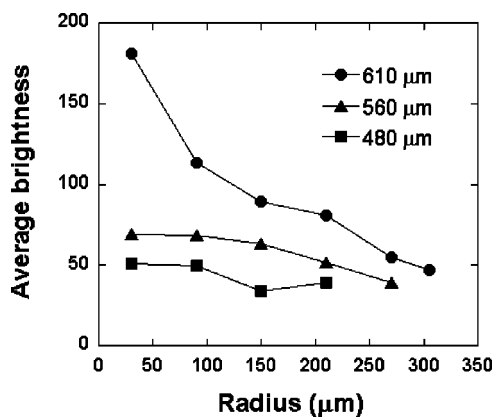


FIG. 4. Average intensities of the holographic features as a function of radius from tumors of different diameters. Larger tumors have features of higher brightness near the center, which is consistent with increasing necrosis in the larger spheroids.

surrounding fluid-filled voids in Fig. 2(b) using transmission electron microscopy.

In contrast to destructive sectioning, coherence-gated holograms provide optical sections noninvasively. Figure 3(a) shows selected sections of one of the OCI data sets obtained for a fresh tumor spheroid (within 1 h of removal from the bioreactor). The data were postprocessed using a high-pass filter along the depth direction ( $z$  direction) of the acquired data to remove static scatter associated with the holographic film. The spheroid has an average diameter of  $660 \mu\text{m}$ . The original data set consists of 200 frames of 180 by 160 pixels with a depth step of  $10 \mu\text{m}$  forming a data cube recording the strongest backscatterers inside the tumor spheroids. A medial cross section of the spheroid is shown in Fig. 3(b). The shadow on the petri dish behind the spheroid allows us to estimate the total thickness of tumor tissue that can be penetrated. The dynamic range of our system allows us to “see” through approximately  $2 \times 600 \mu\text{m} = 1.2 \text{ mm}$  of tumor tissue. The average lateral sizes of the internal structure that we observe is approximately  $50 \mu\text{m}$  for this spheroid, and the longitudinal size was comparable to the coherence length of our laser source. Therefore, the internal structure we observed is consistent with imaging subresolution heterogeneity within the spheroid, presumably the microcalcifications and necrosis. Figure 3(c) shows a three-dimensional (3D) rendering of the structure inside the tumor spheroid.

Using the OCI data, we have analyzed the distribution of necroses inside tumors of different sizes as a function of radius from the center of the spheroid. Figure 4 displays results of histograms of necrotic “intensity” as a function of radius from the center of the spheroids for three tumors with diameters of 610, 560, and  $480 \mu\text{m}$ . While the small tumor spheroid shows a nearly uniform distribution of necroses, the large tumor spheroid has higher intensity near the center of the sample. This is likely due to the difficulty to transport oxygen and nutrients to the center of larger tumor spheroids.

These results are significant because they point out the ability of OCI to differentiate diseased tissue from healthy tissue, which is one of the primary goals of diagnostic imaging.

Our use of holographic coherence imaging shares the full-frame format and the intrinsic spatial resolution of conventional optical imaging. The chief novelty of OCI is its adaptive ability to self-adjust to motion in the system, allowing it to compensate motions during the image acquisition time, removing the need for interferometric stability. This advantage is balanced against the need for the holographic system to absorb light to generate the holographic gratings, thereby presenting an “up-front” cost of approximately 23 dB relative to conventional OCT systems according to theoretical analysis. This trade-off is fundamental, and must be assessed on an application-by-application basis.

In conclusion, we have used a dynamic hologram as a coherence filter that passes coherent image-bearing light to a digital camera, while blocking the usually overwhelming background that obscures the image. The application of the technique to living tumor tissue revealed surprisingly bright structures presumably associated with necroses and calcifications inside rat osteogenic sarcoma tumor spheroids. Correlating the holographic images against conventional microscopic images of the same tumor spheroid is of the utmost importance in the interpretation of the OCI data. It will be particularly important to establish whether the parallel advantage of full-frame acquisition presents additional (or different) features inside the tumor spheroids compared with other coherence-domain techniques.

This work was supported by the National Institutes of Health Award No. R21 RR15040-01.

- <sup>1</sup>B. Chance, *Photon Migration in Tissue* (Plenum, New York, 1989).
- <sup>2</sup>D. Huang, E. A. Swanson, C. P. Lin, J. S. Schuman, W. G. Stinson, W. Chang, M. R. Hee, T. Flotte, K. Gregory, C. A. Puliafito, and J. G. Fujimoto, *Science* **254**, 1178 (1991).
- <sup>3</sup>J. A. Izatt, M. D. Kulkarni, H.-W. Wang, K. Kobayashi, and M. V. Sivak, *IEEE J. Sel. Top. Quantum Electron.* **2**, 1017 (1996).
- <sup>4</sup>J. M. Schmitt and S. H. Xiang, *Opt. Lett.* **23**, 1060 (1998).
- <sup>5</sup>*Handbook of Optical Coherence Tomography*, edited by B. E. Bouma and G. J. Tearney (Marcel Dekker, New York, 2002).
- <sup>6</sup>D. D. Nolte, T. Cubel, L. J. Pyrak-Nolte, and M. R. Melloch, *J. Opt. Soc. Am. B* **18**, 195 (2001).
- <sup>7</sup>S. C. W. Hyde, R. Jones, N. P. Barry, J. C. Dainty, P. M. W. French, K. M. Kwolek, D. D. Nolte, and M. R. Melloch, *IEEE J. Sel. Top. Quantum Electron.* **2**, 965 (1996).
- <sup>8</sup>R. Jones, S. C. W. Hyde, M. J. Lynn, N. P. Barry, J. C. Dainty, P. M. W. French, K. M. Kwolek, D. D. Nolte, and M. R. Melloch, *Appl. Phys. Lett.* **69**, 1837 (1996).
- <sup>9</sup>R. Jones, N. P. Barry, S. C. W. Hyde, P. M. W. French, K. M. Kwolek, D. D. Nolte, and M. R. Melloch, *Opt. Lett.* **23**, 103 (1998).
- <sup>10</sup>M. Tziraki, R. Jones, P. M. W. French, M. R. Melloch, and D. D. Nolte, *Appl. Phys. B: Lasers Opt.* **B70**, 151 (1999).
- <sup>11</sup>D. D. Nolte, *J. Appl. Phys.* **85**, 6259 (1999).
- <sup>12</sup>S. Balasubramanian, I. Lahiri, Y. Ding, M. R. Melloch, and D. D. Nolte, *Appl. Phys. B: Lasers Opt.* **B68**, 862 (1999).
- <sup>13</sup>K. Groebe and W. Mueller-Klieser, *Int. J. Radiat. Oncol., Biol., Phys.* **34**, 395 (1996).
- <sup>14</sup>L. A. Kunz-Schughart, *Cell Biol. Int.* **23**, 157 (1998).
- <sup>15</sup>T. Korff and H. G. Augustin, *J. Cell Biol.* **143**, 1341 (1998).